Adaptive Design Method for a Tilt-Rotor Engine Inlet Duct Optimization

Bambang I. Soemarwoto[1], Remco Habing[1], and Matteo Pecoraro[2]

[1]Royal Netherlands Aerospace Centre NLR, 1059 CM Amsterdam, The Netherlands
[2]Leonardo S.p.A. – Helicopter Division, Cascina Costa di Samarate, 21017, Italy

An adaptive design methodology is presented involving an inverse design to obtain the most possible favorable pressure field in an engine intake duct. A cost functional measuring the deviation between an actual and a desired pressure distribution is to be minimized. A gradient-based optimization algorithm is deployed, where the gradient is calculated by means of the adjoint method. The intake duct has a non-conventional shape that is dictated by an innovative transition mechanism from VTOL to cruise condition (and vice versa) where the position of the engine is kept fixed during tilting of the rotor. The initial design of the duct was rather more dictated by system constraints. Aerodynamically, it features a large distortion on the engine Aerodynamic Interface Plane (AIP) with strong flow unsteadiness. Geometrically, there is a stringent constraint where certain features of the topology of the geometry need to be preserved. An adaptive optimization approach is followed, involving an integrated process from simulation of the complete tilt-rotor configuration for the pre- and post-optimization analyses, to an isolated duct configuration suitable for the design optimization process. The complete configuration includes the rotating blades with rigid pitch-flap motions, nacelle, spinner and wing. The consistency between the complete and isolated domain is ensured by applying proper boundary conditions on the interface between the two domains. The paper will describe the design methodology, process and results in more detail. NLR's CFD code ENFLOW is used throughout the analysis and inverse design process.

I.   Nomenclature

AIP	= Aerodynamic Interface Plane
DC_{60}	= distortion coefficient in a sector of 60 degrees
$\bar{f}_a$	= inertial frame
$\bar{f}_b$	= rotating frame
P_t	= total pressure
q	= dynamic pressure
$r_i(r_o)$	= inner (outer) radius of the AIP
r	= radial coordinate
t	= time
(x_a, y_a, z_a)	= coordinate system in the inertial frame
(x_b, y_b, z_b)	= coordinate system in the rotating frame
ψ_b	= rotation angle of the blade
ψ_f	= angle of the flap motion
ψ_p	= angle of the pitch motion
φ_f	= phase of the flap motion
φ_p	= phase of the pitch motion
θ	= circumferential coordinate
ω	= reduced frequency

II. Introduction

Within the European Clean Sky 2 program for Fast Rotorcraft platform, a Next Generation Civil Tilt-Rotor (NGCTR) demonstrator is being developed. The main benefit of the NGCTR configuration (compared to helicopter and turboprop) is that it offers reduced travel time on short and medium distances , efficiently with respect to rotorcraft architecture. In terms of the FlightPath 2050 goals set by Advisory Council for Aeronautical Research in Europe (ACARE) [1], this architecture contributes to the achievement of the goal that 90% of travellers within Europe are able to complete their journey, door-to-door within 4 hours, where passengers are able to transfer seamlessly between transport modes to reach the final destination smoothly, predictably and on-time.

In order to reduce system complexity and weight, a novel architecture has been proposed, where the position of the engine is kept fixed as the rotor is being tilted from VTOL to airplane mode, and vice versa. This engine integration architecture poses a challenge to ensure a good flow quality that is to be delivered into the engine intake duct under all flying conditions. This entails a good design of the aerodynamic shape of the intake duct, where the focus lies on high efficiency for airplane mode and safe and proper operation in other flight modes.

The design activity involves wind tunnel testing and Computational Fluid Dynamics (CFD) simulations. A full scale model of the intake duct installed within a nacelle configuration has been tested in the wind tunnel, both for the baseline (initial) intake duct geometry and the optimized one, for which CFD has been deployed for the optimization process of the intake duct geometry. The wind tunnel testing for the baseline intake duct has been reported [8]. A second wind tunnel campaign has been conducted and confirmed the improvement achieved by the CFD optimization process.

The aerodynamic design of engine intake duct is a common problem in any gas turbine propulsion system. The design optimization methods can be categorized into gradient-based algorithm (with the adjoint method) and evolutionary or heuristic algorithm. Many past works for optimizing of an S-duct have been reported, e.g. using the adjoint method [9] and genetic algorithms [10]. S-duct is geometry with a simply connected cross section. A more complex intake duct was addressed in the work by Garavello et al. [11] involving a duct which transforms from a simply to multiply connected cross section.

A design methodology for optimization of the engine intake duct having such a multiply connected cross-section is described here. In the pre- and post-design analyses, high-fidelity unsteady time-accurate CFD simulations are deployed to characterize the aerodynamic problems at hand. The adaptive design process involves an inverse design methodology, i.e. a well-known method similar to those described in [6,7] except that here the problem is significantly more complex in terms of constraints, geometry, and definition of the target pressure distribution.

III. NGCTR configuration

Figure 1 depicts a complete configuration of NGCTR that defines the flow domain for the CFD simulation in the airplane mode.
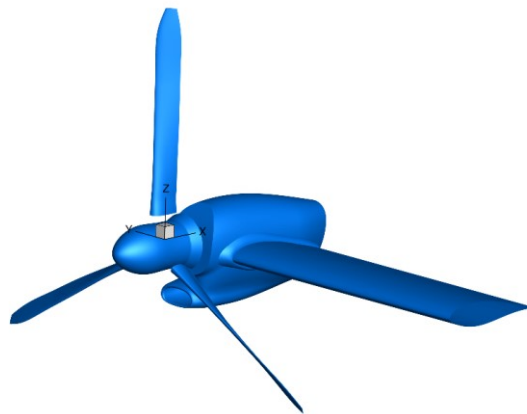
Figure 1 Complete configuration

It involves a global rotating motion of the rotor blades with pitch and flap motions in the local frame of each blade, which can be explained in the airplane mode as follows. The motion of the blade is defined in a multi-body context with two frames of reference:

- The inertial frame (fixed with the aircraft): $\bar{f}_a = (x_a, y_a, z_a)$
- The rotating frame (rotating with the blade): $\bar{f}_b = (x_b, y_b, z_b)$

Initially at $t = 0$, $\bar{f}_b$ is coincident with $\bar{f}_a$. The rotating motions are distinguished into:

- Global motion: blade rotating around the x_a-axis (in airplane mode).
- Pitch motion: blade rotating around an axis radial to the global motion of the blade.
- Flap motion: blade rotating around an axis tangential to the global motion at the blade root.

The state of the global motion is defined by the rotation angle $\psi_b(t)$, which is the angle between z_b-axis and z_a-axis,

$$\psi_b(t) = \omega t \tag{1}$$

where ω is the reduced frequency of the blade rotation. The pitch motion in the rotating frame is written as:

$$\psi_p(t) = \hat{\psi}_p \sin(\omega t + \varphi_p) \tag{2}$$

and afterwards, the flap motion as:

$$\psi_f(t) = \hat{\psi}_f \sin(\omega t + \varphi_f) \tag{3}$$

where $\hat{\psi}$ and φ are the magnitude and phase, respectively.

Due to an innovative transition mechanism from VTOL to cruise condition, and vice versa, a unique topological feature of the intake duct shape has resulted and must be preserved. The duct geometry is an integral part of a complete tilt-rotor configuration consisting of the rotor blades, spinner, nacelle and wing part. The baseline intake duct geometry is illustrated in Figure 2, which also shows that the cross-section geometry of the duct transforms from a simply connected topology at the inlet to multiply connected topology (i.e. an annulus) at the Aerodynamic Interface Plane (AIP). It should also be noted, as it can be observed in Figure 1, the intake duct is located in the vicinity downstream of the rotor blade.

simply connected inlet   multiply connected AIP
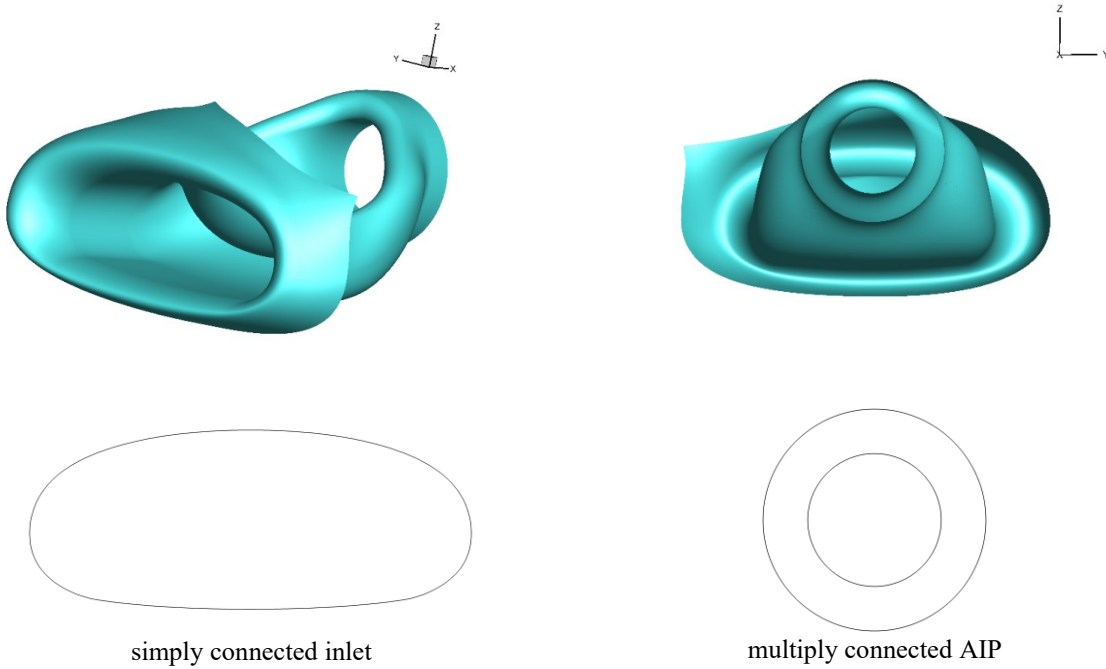
Figure 2 Baseline intake geometry.

IV. CFD method, load cases and grid topology

All the CFD simulations were performed using ENFLOW, which is a high-fidelity CFD code developed in-house at NLR [2]. ENFLOW has been used extensively in various European Projects (e.g. Ref. 3,4) concerning rotating configurations. It solves the time-dependent Reynolds-Averaged Navier-Stokes (RANS) equations in multi-block

structured grids. The two-equation Menter SST turbulence model was used in the simulations performed here. The solution scheme is second-order both spatially and temporally. The unsteady solution procedure employs an implicit dual-time stepping scheme, with a pseudo-time Runge-Kutta integration in combination with a multi-grid scheme is used to achieve a converged solution at each time step. For stability of the integration, artificial dissipation fluxes are added to the physical fluxes.

The flow around the complex geometry shown in Figure 1 must be simulated using the high-fidelity time-accurate CFD method for a large number of load cases. In total there are 15 load cases that need to be evaluated. Each of these load cases has a unique specification of thrust and mass flow, and a unique pitch ($\hat{\psi}_p$) and flap ($\hat{\psi}_f$) motion of the blade. Each simulation has to be trimmed towards the specified thrust of the rotor and mass flow through the AIP. This involves two trim parameters: (i) the blade collective for the thrust, and (ii) the exit static pressure on the exit plane downstream of the AIP.

A flight mode is assigned for each of the 15 load cases (LC), which is either an airplane mode (AP), transition mode (T), or VTOL mode, summarized in Table 1. From one flight mode to another, the spinner and rotor blades have to be rotated around the y-axis, with the nacelle kept fixed. The rotation angle ranges from 0 (in airplane mode), 30, 50, 75 to 90 (in VTOL mode).

Table 1 Summary of the load cases considered.

LC	1	2	3	4	5	6	7	8	9	10	11	12	13	14	15
Mode	Airplane								Transition			VTOL			

In order to allow an efficient CFD simulation procedure, the flow domain is decomposed into a number of domains: stationary and rotating domains. Between two adjacent domains a discontinuous (sliding) interface is defined on which the flow variables are communicated between the two domains by interpolation. The rotating domain is further decomposed into three local domains, each containing a rotor blade as depicted in Figure 3a. Such a tube-like topology is designed to efficiently accommodate a large variation of the collective and pitch angle without impacting the grid quality. The surface of the tube surrounding the blade is an interface that connects the blade domain to the global rotating domain shown in yellow in Figure 3b.

(a) blade domain   (b) global rotating domain
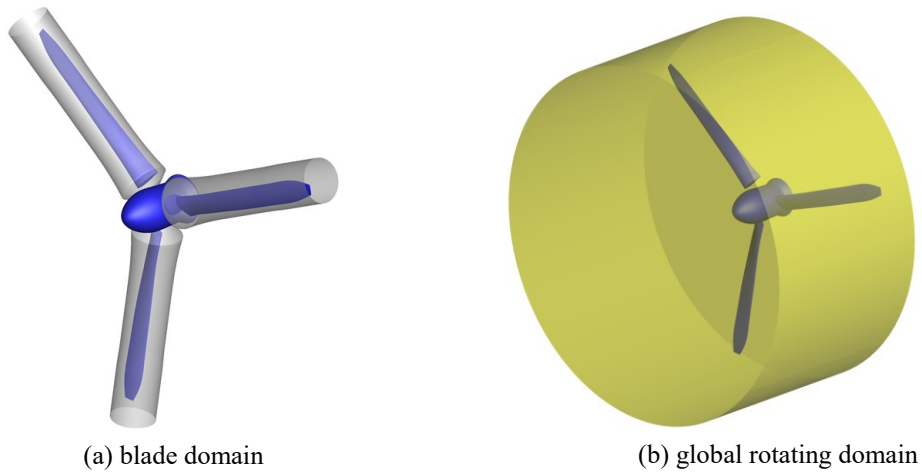
Figure 3 Composition of the rotating domain.

Furthermore, in order to have a versatile way of generating the grid as the flight mode changes between the airplane, transition and VTOL mode, an innovative grid topology has been constructed as shown in Figure 4. With this topology, grid generation can be done efficiently in an automated manner for any tilt angle of the rotor in a range between the airplane mode and the VTOL mode.

(a) airplane mode   (b) VTOL model
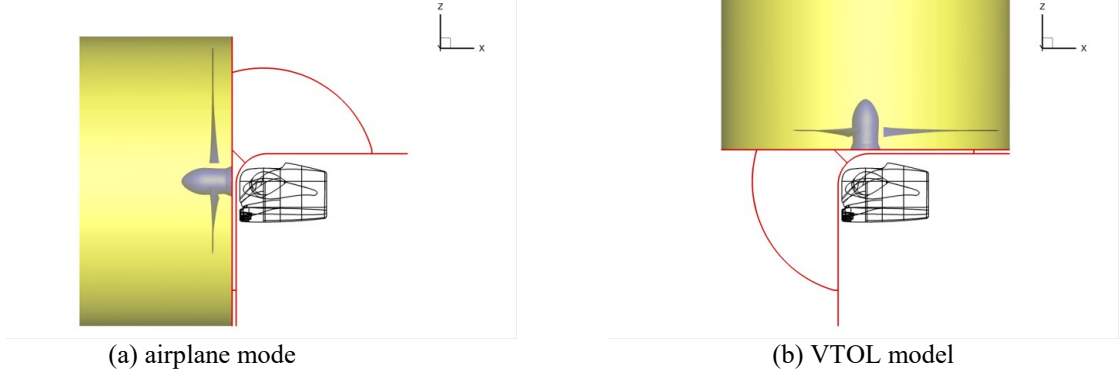
Figure 4 Versatile grid topology.

V.   Optimization problem

The objective of the optimization problem is to minimize the distortion coefficient defined as the maximum DC_{60} on the AIP. The AIP is an annulus with an inner and outer radius of (r_i, r_o), respectively, as depicted in Figure 5.
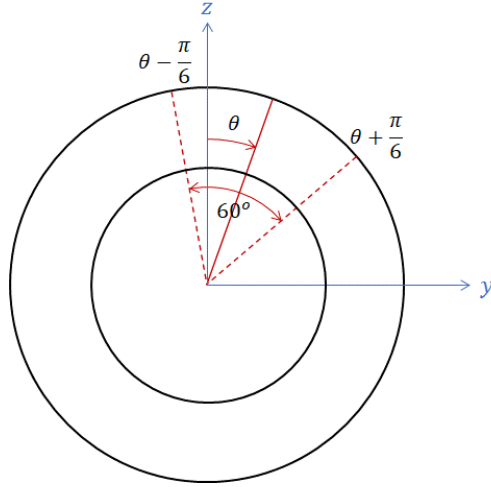
Figure 5 AIP and 60° sector.

The number 60 stands for a sector of 60 degrees at a circumferential location of θ. The value of $DC_{60}(\theta)$ at this location is determined by:

$$DC_{60}(\theta) = \frac{P_{t,A} - P_{t,60,min}}{q_A} \tag{4}$$

where:

$$P_{t,A} = \frac{1}{A} \int_{r_i}^{r_o} \int_0^{2\pi} P_t(r,\theta)\, r\, dr\, d\theta, \qquad \text{the area-averaged total pressure on the AIP,}$$

$$q_A = \frac{1}{A} \int_{r_i}^{r_o} \int_0^{2\pi} q(r,\theta)\, r\, dr\, d\theta, \qquad \text{the area-averaged dynamic pressure on the AIP,}$$

$$P_{t,60,min} = min_{\theta \in [0,2\pi]} \frac{1}{A_{60}} \int_{r_i}^{r_o} \int_{\theta - \frac{\pi}{6}}^{\theta + \frac{\pi}{6}} P_t(r,\theta)\, r\, dr\, d\theta, \qquad \begin{array}{l}\text{the minimum area-averaged total pressure on a}\\ \text{60-degree sector of the whole AIP,}\end{array}$$

with the total A and sector A_{60} areas defined by:

$$A = \int_{r_i}^{r_o} \int_0^{2\pi} r\, dr\, d\theta \,,$$

$$A_{60} = \int_{r_i}^{r_o} \int_{\theta-\frac{\pi}{6}}^{\theta+\frac{\pi}{6}} r\, dr\, d\theta.$$

In the above expressions, P_t is the time-averaged total pressure that is obtained from the unsteady flow solution over a period of time.

The constraints in the optimization problem consist of aerodynamic and geometry constraints. The aerodynamic constraints are specified in terms of radial and circumferential indices of total pressure and total temperature distortion, which are analytically not simple expressions [5]. The geometry constraints are formulated as box constraints defining the areas that must not be penetrated by the surface of the intake duct, as depicted in yellow in Figure 6, with the location of the AIP is fixed.
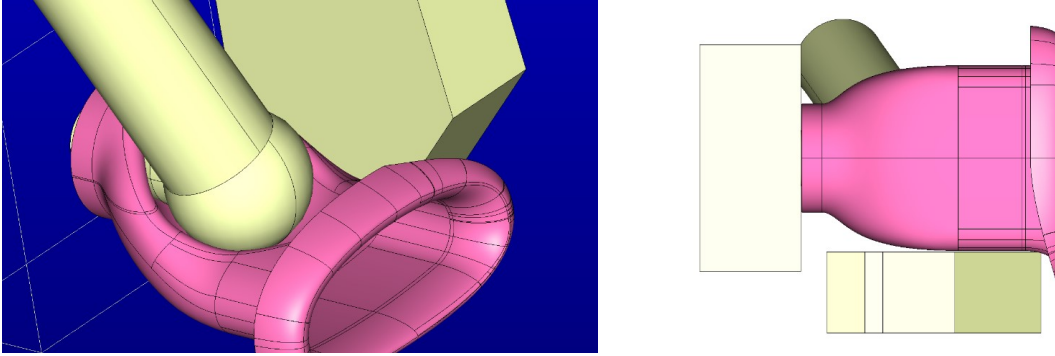
Figure 6 Geometrical box constraints.

VI. CFD simulation

The NGCTR configuration generates aerodynamically complex flow phenomena. It consists of various aerodynamic surfaces that induce different flow mechanisms. In a cruise condition, an interaction between (i) the slipstream induced by the rotor, (ii) the upwash induced by the wing, and (iii) the suction field inside the inlet duct generated by the compressor, determines the flow entering the inlet duct. Similarly, in a VTOL condition, the compressor sucts a flow originating from a downwash field below the rotor. As the nacelle is located between the rotor and the inlet duct, the downwash field is obstructed by the nacelle that in turn may act like a bluff body upstream of the intake duct (see Figure 4b).

The CFD simulations were performed by means of grid sequencing, involving three grid levels: coarse, medium and fine. The boundary layer is assumed to be fully turbulent for all load cases, which is resolved with $y^+ \approx 1$ on the fine grid. Table 2 presents the number of surface grid cells on the most important components of the configuration. The total number of grid cells of the complete configuration is 64.5 million.

Table 2 Surface grid resolution.

Component	n_i	n_j	direction
Rotor	224	72	i – airfoil contour, j – radial
Wing	208	112	i – airfoil contour, j – spanwise
Intake duct	288	288	i – streamwise, j – circumference

A standard setting which defines the temporal resolution and time-span of the unsteady simulation is presented in Table 3. The last one-third rotation of the 3-blade configuration is used for the time-averaging, assuming that the frequency of flow unsteadiness on the AIP due to an upstream flow separation is sufficiently separated from the blade passing frequency, and can be sufficiently captured by 360 samples per blade passing.

Table 3 Temporal resolution and time-span

Grid level	number of time steps / rotation	number of rotations	number of blade passings
Coarse	120	4	12
Medium	180	3	9
Fine	360	2	6

The periodic and grid convergence are assessed based on the mass flow through the AIP and thrust of the rotor. Figure 7 shows a typical convergence during the simulation from the coarse, medium and fine grid, following the scheme shown in
Table 3, for a given value of the collective and the exit static pressure as the trim parameters. It should be noted that the coarse grid may not already be in the asymptotic region of convergence, e.g. because certain flow structures may not be sufficiently resolved in this level. The trimming procedure can be performed on the coarse and medium level, where the resulting collective and exit static pressure are applied with an offset on the fine grid level. Three simulations are usually sufficient to achieve the specified thrust and mass flow. Finally, the flow solution is time-averaged over the last blade passing to allow the calculation of DC_{60} on the AIP.

(a) cost functional   (b) norm of the gradient
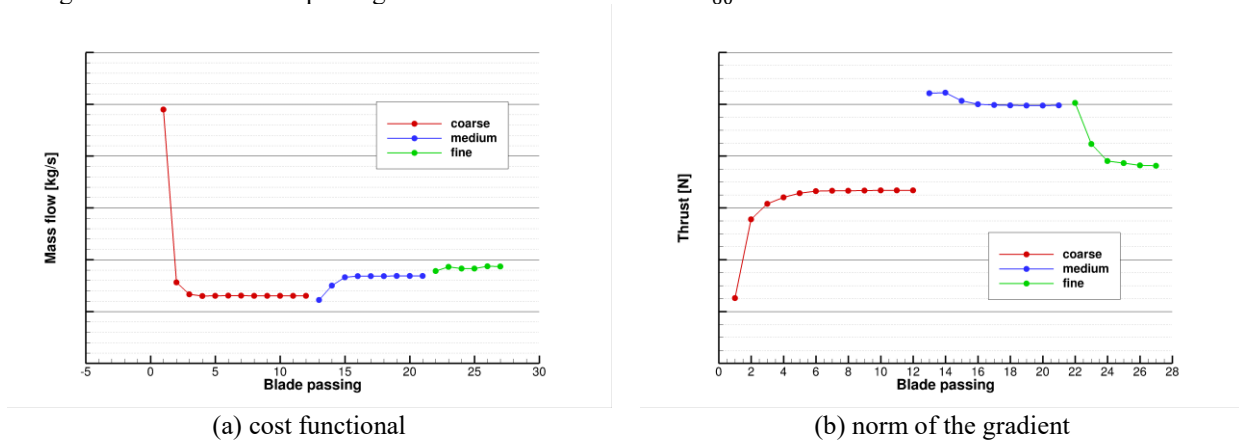
Figure 7 Periodical convergence of the mass flow and thrust.

Figure 8 presents the simulation results for the baseline intake duct in terms of a normalized $DC_{60,max}$ for all the load cases considered. On the left of the figure, the total pressure contours of LC-5, a load case associated with the efficient cruise condition, is shown as an illustration. The region of high distortion on the top sector of the AIP occurs in all load cases, and appears to be associated with the change from a simply to a multiply connected duct topology.
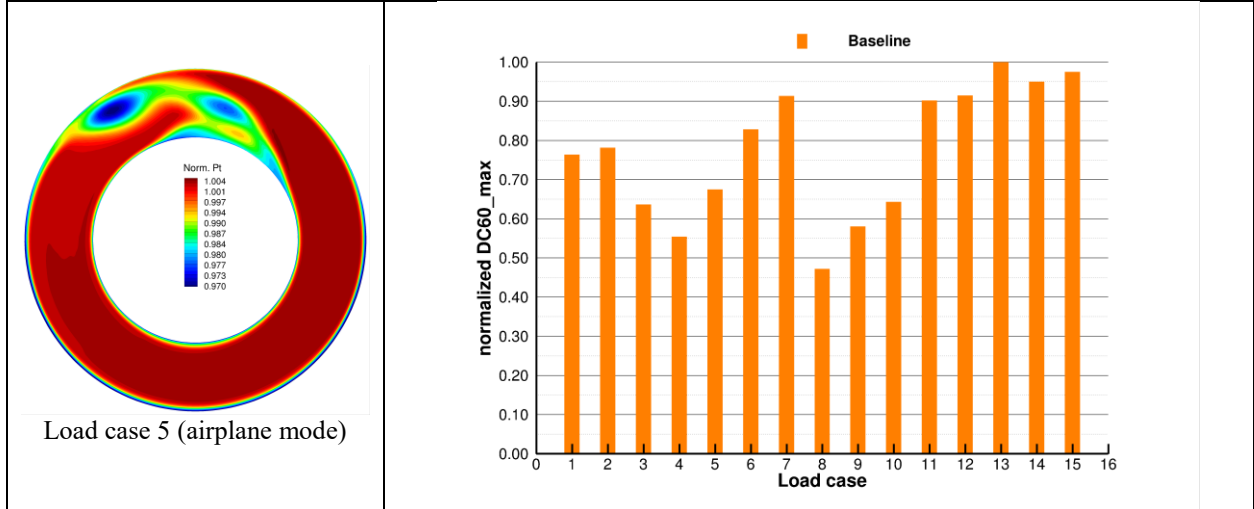
Figure 8 Computational results of the baseline intake duct.

VII. Design scheme

The description in the preceding sections gives a clear idea of a large-scale time-accurate computation that is required to determine the objective function value, $DC_{60,max}$, for one load case and one given geometry of the intake duct. To include such a simulation in a design optimization process will be prohibitively costly. Apart from the large flow domain and various motions that are involved, the problem at hand is even more challenging due to the nature of the unsteady separated flow at the location of interest, i.e. on the AIP.

One may be tempted to simplify the problem by considering only the intake duct, ignoring the other components of the configuration, and subsequently deploy the most advanced optimization algorithm, such as either gradient-based (adjoint methods) or non-gradient-based such as an evolutionary algorithm with surrogate modeling. One may also consider the most advanced geometry parameterization for the intake duct, such as a Free Form Deformation (FFD) shape parameterization. However, the complexity due to the unsteady flow, the influence of the rotor, and the geometry of the intake duct (that is multiply connected and constrained) may preclude such an approach to be effective.

Therefore, as a first step, the duct topology is modified such that the connectivity from the inlet to the AIP is preserved. The new duct geometry is illustrated in Figure 9. This is used as an initial geometry in an inverse design optimization scheme depicted in Figure 10 that is applied to an isolated duct configuration.
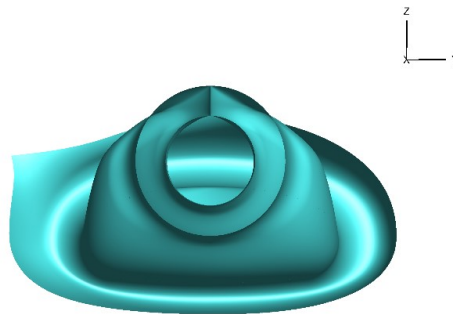
Figure 9 Simply connected intake duct topology.

In order to include the upstream unsteadiness and thrust due to the rotating blades, an interface is defined between the internal flow of the isolated duct and the external flow of the complete configuration as illustrated in Figure 11. On this interface, the unsteady flow quantities obtained from the simulation around the complete configuration are time-averaged and imposed point-wise as a one-dimensional non-reflecting boundary condition for the isolated flow domain. This isolated flow domain is used in the optimization process to obtain an optimum shape of the duct.

8
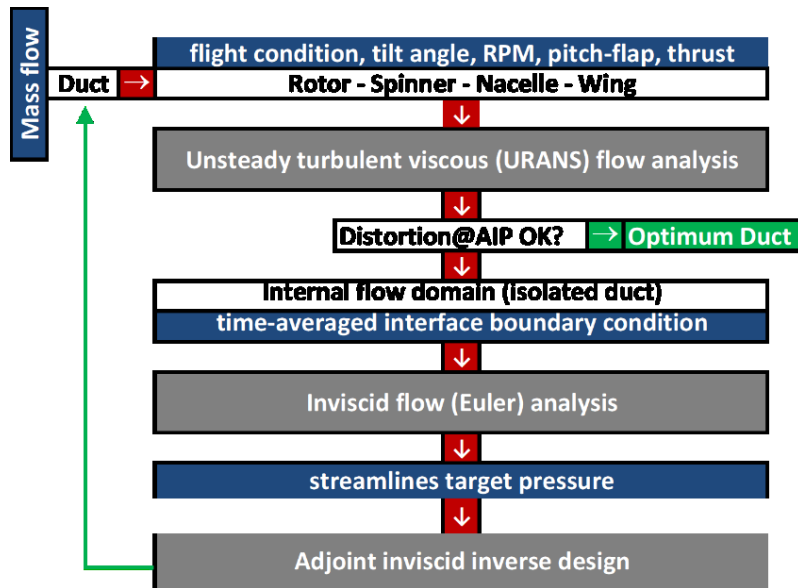
Figure 10 Inverse design optimization scheme.

interface
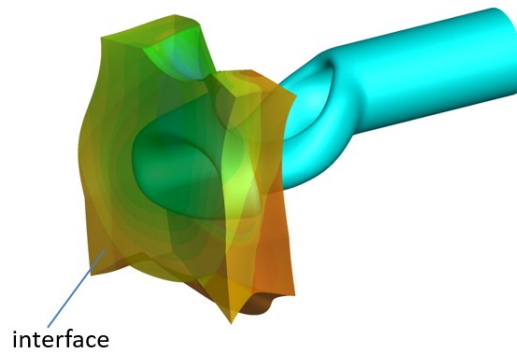
Figure 11 Flow domain of the isolated duct configuration.

A geometrically constrained inverse design procedure is then followed in order to obtain the most favorable aerodynamic characteristics on the AIP. With the boundary condition defined on the interface, a steady inviscid flow model based on the Euler equation is deployed to simulate the internal flow, where the exit pressure is trimmed towards the specified mass flow. Based on the resulting inviscid flow solution, surface streamlines are constructed along which the pressure is extracted. The pressure distribution along the streamline provides a first-order representation of the boundary layer loading.

Upon examination, the pressure distribution is modified towards a desirable one to reduce the boundary layer loading, and therefore inhibit flow separation. After applying this procedure to all streamlines, a target (desirable) pressure distribution on the surface of the duct is specified in a parametric space (s, t) where s is a parametric length in the circumferential direction, while t in the axial direction, of the intake duct. Figure 12 shows a target pressure distribution in comparison with the current actual one, where adverse pressure gradients have been eliminated. It should be noted that the target pressure distribution does not have to be necessarily realizable. It serves only the purpose of steering an actual pressure distribution towards a more desirable one to inhibit flow separation.

(a) current (actual) pressure distribution

(b) target pressure distribution
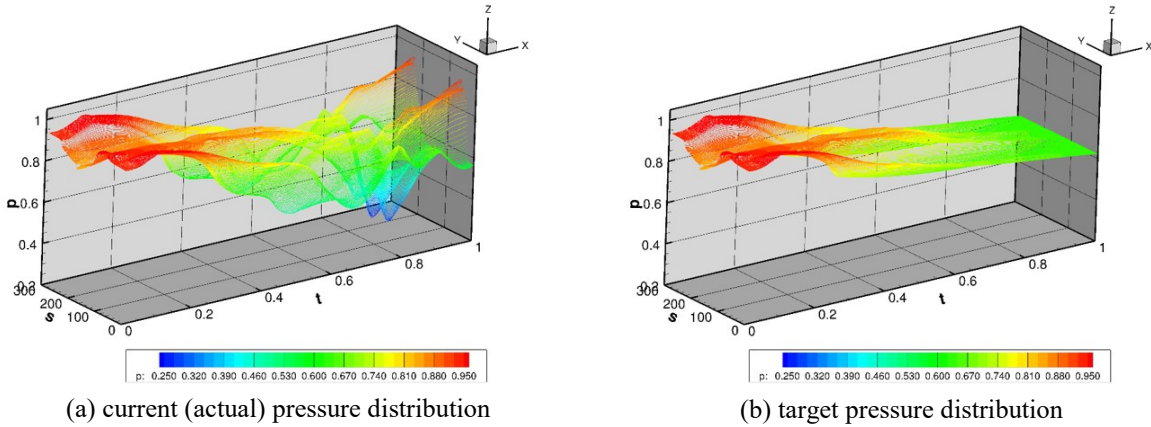
Figure 12 Current and target pressure distribution.

A cost functional is defined giving a measure of the deviation between the actual and target pressure distribution. The deviation is minimized in a least-square sense by updating the geometry subject to the box constraints. The minimization problem is solved by means of a gradient-based optimization algorithm, where the gradient is calculated efficiently by means of the adjoint method. Figure 13 shows the history of the inverse design optimization process, where both the value of the cost functional and its gradient norm have been reduced. This iterative procedure results in a new duct shape that is to be integrated into the complete configuration.
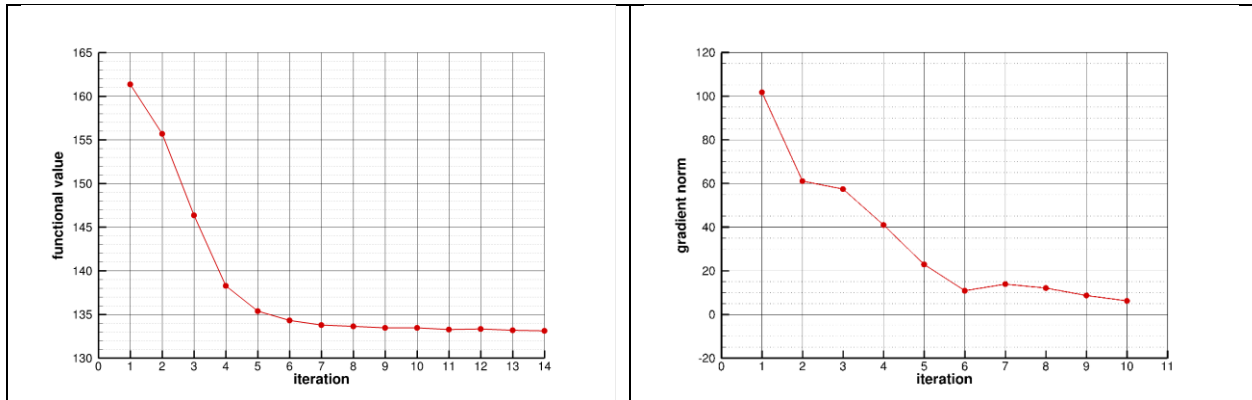
Figure 13 History of the inverse design optimization process.

The unsteady simulation procedure of the complete configuration is repeated to determine the impact of the design optimization process. For reasons of efficiency, simulations for the intermediate geometries were performed on the medium grid level. Figure 14 demonstrates a significant improvement for LC-5 that has resulted from the whole process, starting from (a) the baseline, to (b) the geometry with the new duct topology, and finally (c) the geometry produced by the inverse design process. On the medium grid level, the reduction in $DC_{60,max}$ from (a) to (b) due to the change in the topology is 73%, while from (b) to (c) due to the inverse design is 37%.

10

(a) baseline duct   (b) simply connected duct   (c) result of inverse design
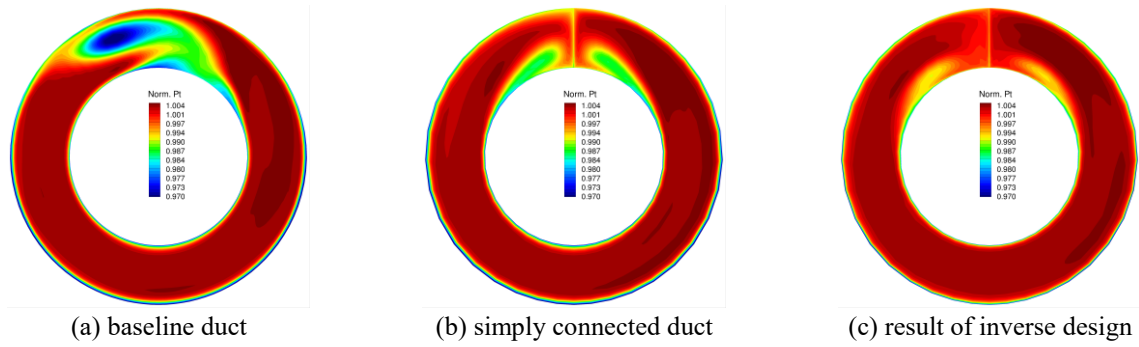
Figure 14 Aerodynamic improvement on the medium grid.

Finally, a full-fledged assessment was performed on the fine grid level for the complete configuration to quantify the impact of the design optimization. The reduction in $DC_{60,max}$ for LC-5 is 80% which is in line with a significant improvement in the total pressure contours on the AIP. The new flow topology was found to be stable that is nearly steady. The optimum geometry has also brought a significant reduction of $DC_{60,max}$ in all load cases considered.
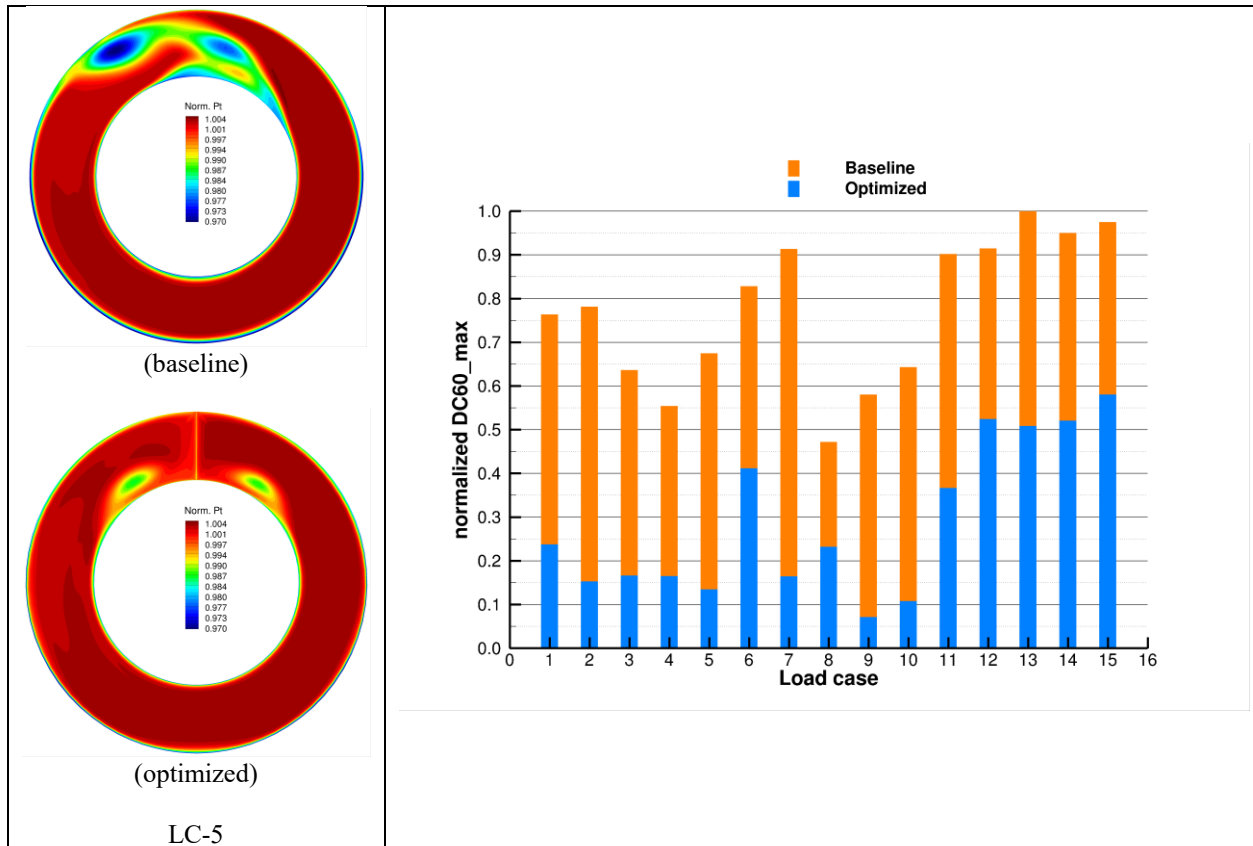
Figure 15 Impact of the design optimization.

VIII. Wind tunnel testing

Wind tunnel testing has been conducted in the DNW-LLF wind tunnel for both the baseline [8] and optimized intake duct geometry. The rotor blades are excluded to allow a full-scale intake duct geometry to be accommodated in the

test section. An impression of the 6 by 6 meter test section is shown in Figure 16. Not all load cases have been evaluated. The similarity between the numerical CFD and experimental wind tunnel conditions are ensured by the same Reynolds number based on the AIP bulk flow condition and the Inverse Capture Ratio (ICR). Figure 17 presents a comparison of the impact of the design optimization as predicted by CFD and as measured in the wind tunnel.

Figure 16 DNW-LLF test section with a full-scale intake geometry.
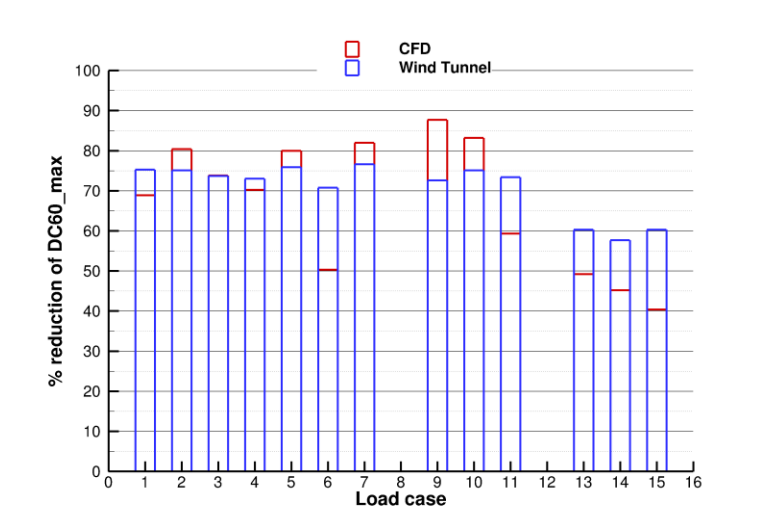
Figure 17 Comparison of reduction of $DC_{60,max}$ between CFD and wind tunnel.

IX. Conclusions

A design problem of the engine intake duct of a tilt-rotor configuration has been addressed. The quantitative assessment of the intake duct entails a large-scale high-fidelity unsteady time-accurate CFD simulation. A design optimization methodology has been presented, comprising the whole process of flow analysis, evaluation of the objective, and stages of the design process. The methodology has been demonstrated to be effective to produce a significant improvement of the intake duct that is confirmed by wind tunnel testing.

Acknowledgments

References

[1] Report on the Aeronautical Research Activities and Capabilities of New Member States of the European Union. Advisory Council for Aeronautical Research in Europe (ACARE) Member States Group WT6, 2007. Available online: https://www.airtn.eu/downloads/report-on-the-aeronautical-research-activities.pdf.

[2] Kok, J.C. "A high-order low-dispersion symmetry-preserving finite-volume method for compressible flow on curvilinear grids", *Journal of Computational Physics*, 228 (2009) 6811-6832.

[3] Meheut, M., Sartor, F., Vergez, M., Laban, M., Schnell, R., Stuermer, A.W., and Lefevre, G., "Assessment of Fan/Airframe aerodynamic performance using 360° URANS computations: Code-to-Code comparison between ONERA, DLR, NLR and Airbus", AIAA 2019-0582.

[4] Tom Stokkermans, Leo Veldhuis, Bambang Soemarwoto, Raphaël Fukari, Paul Eglin, "Breakdown of aerodynamic interactions for the lateral rotors on a compound helicopter", Aerospace Science and Technology, Volume 101, June 2020.

[5] SAE-ARP1420 C: Gas Turbine Engine Inlet Flow Distorsion Guidelines, Rev. C. April 2017.

[6] Laban, M. Soemarwoto, B.I., and Kooi, J.W., "Reshaping Engine Nacelles for Testing in Wind Tunnels with Turbofan Propulsion Simulators", AIAA Paper 2005-3703, July 2005.

[7] Soemarwoto, B.I., Boelens, O.J., and Kanakis, A., "Aerodynamic design of gas turbine engine intake duct", *Aircraft Engineering and Aerospace Technology*, Vol. 88 No. 5, pp. 605-612. https://doi.org/10.1108/AEAT-02-2015-0063.

[8] Habing, R., Philipsen, I., Müller, M., Pecoraro, M., "Experimental Evaluation Of Flow Distortion At Tilt-Rotor Full-Scale Model Air Intake Wind Tunnel Test", 47th European Rotorcraft Forum, paper 20, 7-9th September, 2021.

[9] Kamat, V., Rao, V., Xu, M., and Saxena, S., "Flow Distortion Based S-Duct Optimization using Adjoint Methodology", AIAA paper 2020-2755.

[10] Furlan, F., Chiereghin, N., and Kipouros, T., "Computational design of S-Duct intakes for distributed propulsion", Aircraft Engineering and Aerospace Technology, 86/6 (2014) 473–477, https://doi.org/10.1108/AEAT-04-2014-0046.

[11] Garavello, A., Benini, E., Ponza, R., Scandroglio, A., and Saporiti, A., "Aerodynamic Optimization of the ERICA Tilt-Rotor Intake and Exhaust System", Paper ERF-191, 37th European Rotorcraft Forum, September 13th – 15th, 2011, Ticino Park, Italy.